Control of Magnetic Behavior in $LaMnO_3$ Thin Films through Cationic Vacancies

A Thesis

Submitted to the Faculty

of

Drexel University

by

Cerina Gordon

In partial fulfillment of the

requirements for the degree

of

Master of Science in Materials Science and Engineering

June 2017

Acknowledgements

I would like to express thanks to all those who helped me and stood by me during the production of this work. In particular I'd like to thank Mark Scafetta and Dr. Steve May for providing the opportunity to study this problem, Mark for growing the films and Dr. May for prompting the study of this problem and providing the resources to study it. Growth of the films by Mark S. was funded by the National Science Foundatin (DMR-1151649)

I'd also like to thank my lab group for providing training on several of the tests performed, assisting in characterization and providing useful discussion and moral support. Similarly, I'd like to thank my committee members, Dr. Steve May, Dr. Goran Karapetrov and Dr. Garritt Tucker for the valuable discussion following my defense.

Finally, I'd like to thank my friends and family for providing support and sticking it out with me, and providing an outside perspective to remind me of exactly what a general audience does and does not know.

Table of Contents

List of Tables

List of Figures

Abstract

Control of Magnetic Behavior in $LaMnO_3$ Thin Films
through Cationic Vacancies
Cerina Gordon

The magnetic behavior of lanthanum manganite thin films ($LaMnO_3$) deposited on strontium titanate ($SrTiO_3$) was explored as a function of manganese oxidation state, as controlled by the presence of cation and oxygen vacancies. This was done in response to the inconsistent magnetic properties found in literature. The films were characterized using Rutherford backscattering spectroscopy, wide-angle x-ray diffraction, x-ray reflectivity and vibrating sample magnetometry. The films were found to exhibit an antiferromagnetic to ferromagnetic transition consistent with that found in strontium-doped $LaMnO_3$ systems, where the manganese oxidation state is controlled by the fraction of strontium present.

1. Introduction

Thin film magnetic devices have revolutionized data storage in much the same way thin film semiconductor devices have revolutionized computing. Between 1990 and 2005, hard drive data storage areal density increased from 100 Mbit/in^2 to 110 Gbit/in^2. This was accompanied by a 1000-fold decrease in data storage price per byte. This regular improvement was called Kryder's law, as an analogue to Moore's law, describing the exponential increase in areal density of transistors. [1]

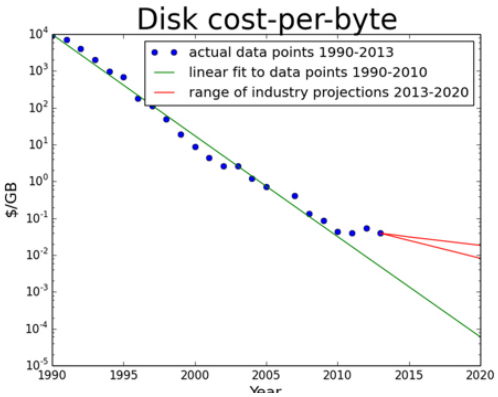

Figure 1.1 Slowdown in hard-drive improvements, as compared to predictions a la Kryder's law. [2]

In recent years, this projected increase in areal density has slowed as hard drive technologies approach fundamental limits. Continued improvements rely on the development of new technologies, including changes to hard drive architecture, changes to data storage mechanism and improvements to the material systems being used.

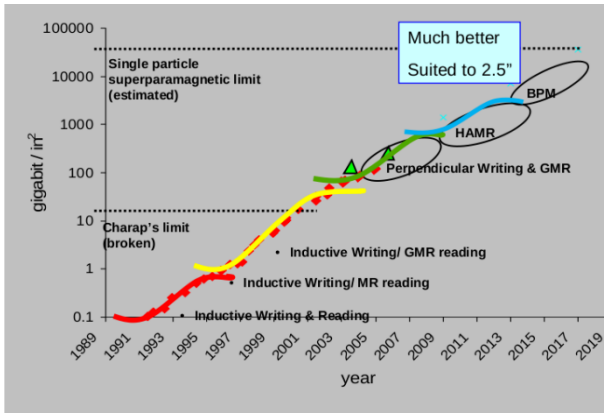

Figure 1.2 Seagate's 2008 technology roadmap for continued improvements in hard drive storage capacity. Heat-assisted magnetic recording (HAMR) has not yet been realized in a consumer product. [2]

One of the biggest advances in hard drive storage capacity in recent years was due to the development of perpendicular writing. In this configuration bits are magnetized

perpendicular to the platter surface, rather than the parallel orientation used in the past. This technology relies on several exotic behaviors including giant magnetoresistance. Additionally, layers with a variety of well-controlled magnetic behaviors are required, including layers showing soft ferromagnetism and antiferromagnetic behavior. Use of this technology moves the theoretical maximum areal density for magnetic hard drives from ~100 Gbits/in^2 to over 500-600 Gbits/in^2. [4]

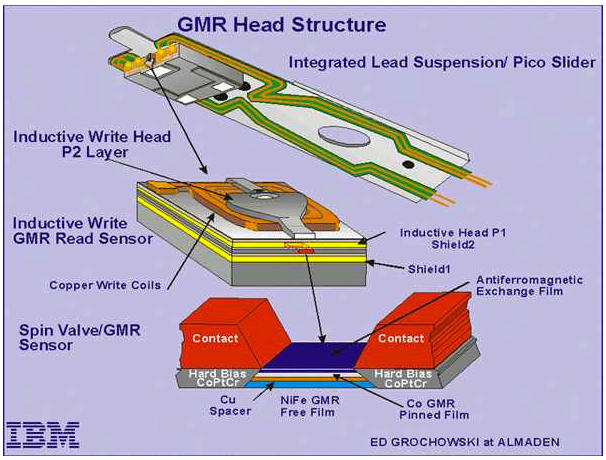

Figure 1.3 IBM hard drive architecture for perpendicular writing. [3]

In addition to driving a need for the development of a variety of magnetic materials, thin films and heterostructures, the development of perpendicular writing illustrates the need for continued research into basic physical phenomena such as those that form the basis of the emerging field of spintronics. A material system that has gained interest is that of perovskite oxides, as they are massively tunable due to a large number of degrees of freedom and many compounds exhibit exotic behaviors such as superconductivity and ferroelectricity. [5]

One material, lanthanum manganite ($LaMnO_3$), when grown as a thin film, can be tuned from antiferromagnetic to ferromagnetic under a wide variety of circumstances using a range of techniques. The characterization and origin of this behavior is explored within this work.

2. Background

Magnets and Magnetization

Definition of a Magnet

Magnetic materials are any materials whose electrons align themselves in response to an applied external magnetic field. These materials can be classified into several broad categories: ferromagnetic, antiferromagnetic, ferrimagnetic, paramagnetic and diamagnetic. These categories represent distinct frameworks for ordering with implications with regards to their magnetic susceptibility, spin exchange energy and magnetic domain structure as well as macroscopic properties such as their saturation magnetization and coercivity.

The origin of magnetism is the motion, and internal angular momentum, of electrons. According to Ampere's Law,

$$\nabla \times B = \mu_0 J \qquad (2.1)$$

where B is a magnetic field, μ_0 is the vacuum permeability constant and J is total current density, electric currents create magnetic fields. By using the definition of current as the flow of charged particles it can be seen that there is a current associated with the motion of a single electron. Thus, electrons in orbitals can lead to the exhibition of an orbital moment. The intrinsic magnetic moment of an electron, independent of its orbital motion, is called an electron's spin, and has a magnitude of one Bohr magneton. While electrons in filled orbitals will pair up such that these moments nullify one another, according to Hund's rules, electrons in partially empty orbitals will align their spins to maximize their collective spin angular momentum, maximizing their collective magnetic moment. These small

moments can, depending on various material properties, align with the moments of electrons orbiting adjacent atoms, resulting in macroscopic magnetic behavior.

Types of Magnetic Behavior in Materials

When examining magnetism on this atomic scale it is possible to define the five previously mentioned types of magnetism by how adjacent spins align after application and removal of an applied magnetic field: in ferromagnetic materials adjacent spins align parallel to one another, in antiferromagnetic materials adjacent spins of equal magnitude align opposite one another, in ferrimagnetic materials adjacent spins of unequal magnitudes align opposite one another with the larger spins aligned. The spins in paramagnetic and diamagnetic materials do not align without an applied magnetic field, but while a field is applied paramagnetic materials show a slight net moment in alignment with the applied field, while diamagnetic materials show a slight moment opposed to the applied field.

Table 2.1: Categorization of magnetic materials by alignment of adjacent spins

	Alignment of adjacent spins	Net Magnetic Moment
Ferromagnetic	↑↑↑↑↑↑↑↑↑↑	large, +
Antiferromagnetic	↑↓↑↓↑↓↑↓↑↓	zero
Ferrimagnetic	↑↓↑↓↑↓↑↓↑↓↑↓	meduim, +
Paramagnetic	~	small, +
Diamagnetic	~	small, -

This aligned-opposed behavior is typically modeled with a parameter called exchange energy, representing the energy associated with aligning spins between adjacent atoms and defined as

$$\varepsilon_{ex} = -JS_i \cdot S_j \qquad (2.2)$$

where $S_i \cdot S_j$ represents the relative angle between adjacent spins and J represents the exchange integral, which is a material property. If J is positive then there is a reduction in energy for $S_i \cdot S_j > 0$, which corresponds to aligned spins, with a minimum at $S_i \cdot S_j = 1$, the vectors being exactly parallel. This is the definition for ferromagnetic materials. Similarly, for negative J the lowest energy configuration is for adjacent spins to line up opposite one another, this being the case in antiferromagnetic and ferrimagnetic materials.

The alignment behavior of adjacent spins becomes entropy-controlled at higher temperatures, with the temperature being dependent on the magnitude of the exchange integral. Above the temperature at which behavior becomes entropy-controlled, ferromagnetic, ferrimagnetic and antiferromagnetic materials become paramagnetic. In ferromagnetic materials this transition temperature is called the Curie transition temperature; in antiferromagnetic materials this is the Néel temperature. In addition to the observation of the disappearance of spin ordering, this transition may be observed as a discontinuity in the first derivative of a material's magnetic susceptibility.

Magnetic susceptibility is defined as the ability for an external field to magnetize a sample,

$$M = \chi B \qquad (2.3)$$

where M is the magnetization of the sample, B is the applied field and χ is the susceptibility. This is a bulk property which changes with temperature, in accordance with the relationship to entropy/exchange energy described above, and is distinct for each of the previously described types of magnetic behavior. In paramagnetic and diamagnetic materials, this property is typically constant with respect to temperature and applied field, being a positive constant in paramagnetic materials and negative in diamagnets. Magnetization, and therefore susceptibility in antiferromagnetic materials is small, increasing with temperature to reach a sharp peak at the Néel transition. Magnetization in ferromagnetic materials is more complicated and as a result susceptibility is a non-linear equation. [6]

Ferromagnetic Behavior

In ferromagnetic materials, an applied field may cause all the unpaired spins to become aligned with that field; with no more spins to align, magnetization cannot increase and susceptibility becomes essentially zero. The degree of magnetization in this condition is called the saturation magnetization. This can be seen in both the formation and development of their domain structure and the shape of magnetic moment vs applied field graphs.

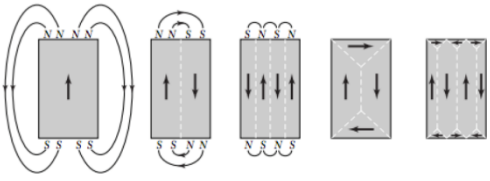

Figure 2.1 Alignment and growth of magnetic domains in a ferromagnetic material. The left-most sample has reached saturation magnetization. Repurposed from [6]

The unpaired spins in ferromagnetic materials show local alignment within regions called domains. These domains vary in size and alignment direction. Prior to application of a magnetic field these domains are randomly oriented, with their net moment typically

summing to zero across the sample. On application of a magnetic field, the domains aligned with the field grow while those aligned oppositely shrink, resulting in a net magnetic moment in the direction of the applied field.

When a magnetic field is applied to a non-magnetized sample, a linear increase in magnetization is observed, similar to that observed in paramagnetic materials. At some applied field this magnetization will reach a maximum which, when normalized with the number of contributing atoms in the sample, is slightly less than 1 μ_B per unpaired electron per atom. For example, nickel in its ground state has an electronic configuration of $3d^8\ 4s^2$, meaning it has 2 unpaired electrons in its d-shell. This corresponds to a theoretical maximum magnetization of 2 μ_B/Ni. On removal of the applied field the magnetization of the sample will decrease linearly, similar to the path seen when the field was initially applied. However, the sample will retain some net magnetization at zero applied field, called the remanence; without any driving force the domains will remain aligned. Some field, called the coercive field, must be applied in the other direction to return the sample to zero magnetization. Further application of a magnetic field in the opposite direction results in the same saturation behavior seen in the other direction.

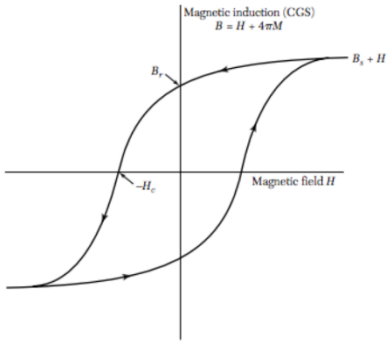

Figure 2.2 Typical magnetic moment (M) vs. applied field (H) behavior for ferromagnetic materials. Repurposed from [6]

Antiferromagnetic Behavior

While there is only one way of arranging spins so that adjacent spins have opposite orientations in 1D space, when moving to 2D or 3D space more configurations become available. For example, three forms of ordering in antiferromagnetic materials are: A-type, representing parallel alignment in 2 axes, antiparallel in the third, C-type, representing parallel alignment in 1 axis, antiparallel in the other 2, and G-type, antiparallel alignment in all 3 axes. As a result, it is possible to have a net magnetic moment along one axis or within a plane while having no net magnetization across the entire sample. However, the magnetic moment observed in most antiferromagnetic materials is the result of a different phenomenon called spin canting. Spin canting refers to a slight ($<30^0$) off-axis tilt which can appear systematically throughout a sample. As in ferromagnetic materials it is possible for the moments arising from spin canting to negate one another across the sample or to be aligned via application of a magnetic field, resulting in a small net magnetization and ferromagnet-like behavior.

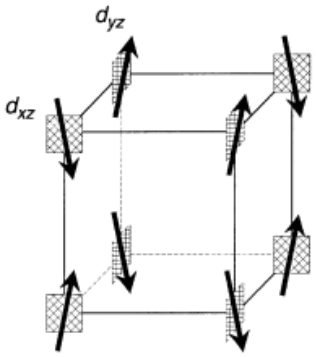

Figure 2.3 Example spin canting in a G-type antiferromagnetic material. This material would show a slight magnetic moment in the positive x direction. Repurposed from [7]

Perovskites

Perovskites are materials with the general chemical formula ABX_3 where A and B are cations, A being larger than B, and X being oxygen, nitrogen, carbon, hydrogen or a halogen gas. [8] [9] As the oxide is the most common form it is the only one that will be mentioned here forward. The cation on the A-site is of an element that can take the oxidation states +1, +2, +3 or some combination of those, while the cation on the B site is generally a transition metal.

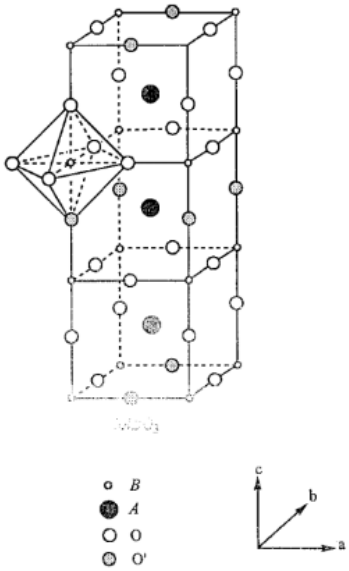

Figure 2.4: Crystal structure of an ideal perovskite. Repurposed from [9]

These materials are distinguished from other materials of matching composition by their crystal structure: crystals in this group typically take the cubic structure, which may be represented as corner-sharing octahedra with B-cations in the center and A-cations in the vacancies between clusters, or as cubic crystals with an A cation in the body center location, B cations at the corners and oxygen at the center of each edge. While the material can take on an orthorhombic, rhombohedral or tetragonal structure [8] the relative positions of these atoms remains mostly constant.

Charge balancing

Perovskites are typically described as ionic solids, meaning the atoms are fully ionized and the formula may be charge balanced in order to determine the oxidation states of the individual components. As oxygen can only take the oxidation state -2, this is the

starting point. The sum of the oxidation states of the A and B cations is therefore +6, as there are 3 oxygens per formula unit. Since B is frequently transition metals which can take on multiple oxidation states, mixed oxidation states are frequently observed, for example $B_x^{+3}B_{1-x}^{+4}$, or $B^{3.5}$. The properties of materials exhibiting mixed oxidation states vary depending on whether or not the ions exhibiting a given oxidation state are fixed to that oxidation state and ordered; some materials exhibit a transition temperature below which these ions are ordered.

Defects

These materials can be tailored through a variety of means including the addition of substitutional groups on either the A site or the B site, resulting in the formula $A1_xA2_{1-x}B1_yB2_{1-y}O_3$, nonstoichiometry on the oxygen site, resulting in the formula $ABO_{3-\delta}$, or deficiency on either of the cation sites, resulting in the formula $A_{1-\delta1}B_{1-\delta2}O_3$ [10]; this last defect is commonly represented with the formula $ABO_{3+\delta}$, however there is very little room in the crystal structure to accommodate interstitial oxygen making the presence of excess oxygen unlikely [10]. Conversely, oxygen deficiency is very common and can be widely accommodated. In fact, the brownmillerite structure exhibited by materials with the formula $A_2B_2O_5$ is the perovskite structure with ordered oxygen vacancies. Oxygen and cation deficiency may be accommodated for through oxidation or reduction of one or both cations, more frequently the B-site cation. Additionally, cation deficiency can be accommodated through an equivalent amount of oxygen deficiency. [9]

Magnetic and Electronic Behavior in Perovskites

Electronic Orbitals

The orbit of an electron around a nucleus can be described through the use of 4 quantum numbers, the principle quantum number (n), angular quantum number (l), magnetic quantum number (m) and spin quantum number (m_s). The principle quantum number refers to the "shell" the electron falls into. The angular quantum number dictates the shape of the electron's orbital, where these shapes were originally derived from Schrödinger's equation and have since been imaged in various ways. These two numbers can be combined as in $1s^2$ to compactly display the approximate energy and shape of an orbital, as well as the number of electrons in that orbital. In the previous example, there were 2 electrons in the 1^{st} "s" orbital showing that configuration. Generally, when describing the electrons orbiting an element only the outermost electrons are shown as these are the electrons which might interact with a neighboring atom. When not shown the remainder of the electrons have the same configuration as those in the noble gas from the preceding row of the periodic table.

Electron Energy Levels

Each set of quantum numbers an electron can have is associated with a certain energy, with higher numbers having higher energies. A very simplified way of showing this is by drawing the energy levels as grouped sets of parallel horizontal lines which electrons can be placed onto, represented as arrows.

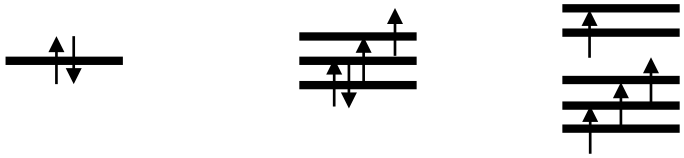

$1s^2$ $2p^4$ $3d^4$

Electrons fill from the lowest energy level to the highest. Each energy level will host a single electron, with all electrons spinning in the same direction, before electrons begin to form pairs spinning in opposite directions. Entire orbitals fill before other orbitals become accessible, such that only one orbital will be partially filled at any given time.

Electron Configuration in Oxides

The atomic configuration of oxides can be represented in 1D as two cations with valence electrons separated by an oxygen anion, with the outermost electron shell being $2p^6$. As this represents a filled valence shell, which is highly stable, these electrons do not move. However, the p-orbital may be oriented along any given axis to minimize the total energy of the system.

The shape of the outermost shell on the cations tends to be more complicated and varied, particularly in the case of transition metals where the outermost orbital is a d-orbital. For transition metal oxides, these electrons may be oriented in either the t_{2g} state, maximizing the distance between d and p electrons and thus reducing their

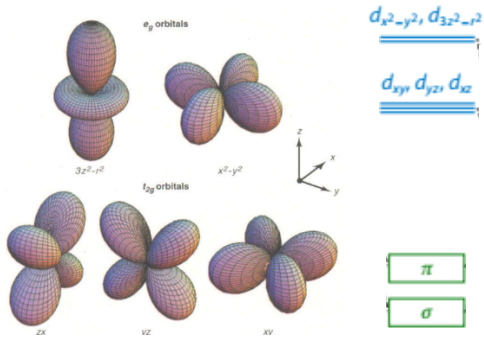

Figure 2.5 d-orbitals and corresponding energy levels. π corresponds to the p-orbitals, σ corresponds to the s-orbital. Repurposed from [27] and [8] respectively

energy, or the e_g state, allowing electron delocalization and transfer. This results in two distinct sets of energy levels, 3 lower-energy t_{2g} states and 2 higher-energy e_g states.

Considering a material containing cations showing mixed oxidation states several linear combinations become possible. For example, considering an Mn – O – Mn system in which Mn can take the oxidations states +3 or +4, the following configurations are possible:

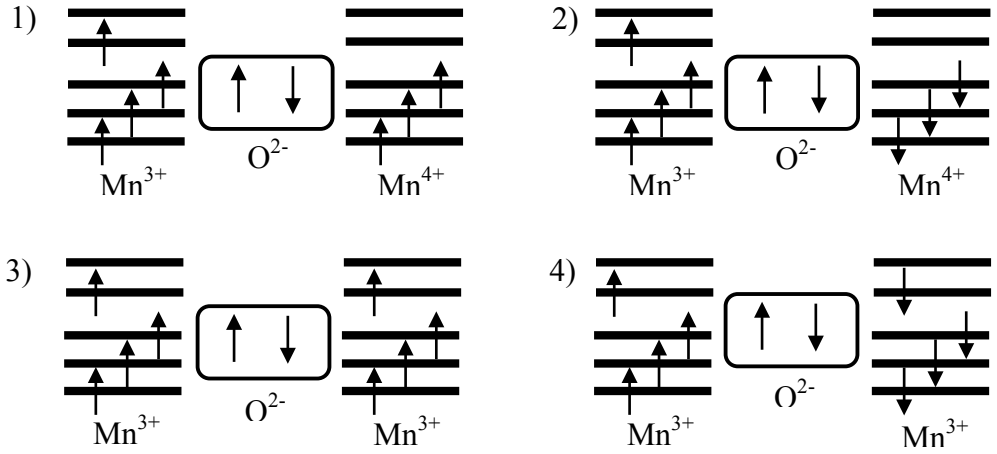

Mn^{3+} has four valence electrons in the 3d orbital, Mn^{4+} has three valence electrons in the 3d orbital. O^{2-} has a filled valence shell, not shown. Mn^{4+} - O - Mn^{4+} interactions are also possible, however the selection rules for magnetism are identical to the Mn^{3+} - O - Mn^{3+} case, so it is not shown.

Each of these configurations suggests a type of magnetism and a relative amount of overall energy. Configurations 1 and 3 correspond to ferromagnetic ordering, as adjacent manganese atoms show parallel spin ordering, while configurations 2 and 4 show antiferromagnetic ordering. In real crystals only configurations 1 and 4 appear, as these configurations allow the electrons to delocalize the most without changing their spin states.

Behaviors in Perovskites

Owing to the wide degree of tunability in both the chemistry and structure of perovskites, a wide range of behaviors may be observed in this family of materials. When considering magnetism, the electrons occupying the d-orbitals of the B-site transition metal cations are of particular interest as these orbitals are generally only partially filled and can be localized to sit almost entirely on one plane or along one axis. Additionally, the BO_6 octahedron can be tilted or distorted, altering the orientation and energy of these electrons. [10]

Lanthanum Manganite

Bulk $LaMnO_3$

Bulk lanthanum manganite takes the perovskite structure, space group Pbnm. It is typically orthorhombic with a pseudocubic lattice parameter of 3.932 Å, where this lattice parameter corresponds to the distance between manganese atoms; lattice parameter can refer to different distances depending on how you define the unit cell. The crystal experiences a Jahn-Teller transition at 750 K. This distortion is asymmetric and periodic, yielding two new manganese-manganese distances, 3.982 Å along the a and b axes and 3.834 Å in the c axis [10]. It is an A-type antiferromagnetic material with a transition temperature near 140 K [10] [11] [12], showing a saturation magnetic moment of 0.18 μ_B/Mn at 10 K [10] [11]. It can accommodate a wide range of both oxygen and cation vacancies.

On removal of enough oxygen, $LaMnO_{3-\delta}$, $0.2 \leq \delta \leq 0.25$, a second orthorhombic phase appears, showing a GdFeO3-type structure. This phase shows a saturation magnetic moment of ~1.5 μ_B/Mn at 8K [12]. Similarly, the presence of cation vacancies has been shown to be linked to the presence of a ferromagnetic phase for $\delta \geq 0.025$, where δ represents the equivalent amount of oxygen excess for some amount of cation vacancies, $LaMnO_{3+\delta} = La_{1-\varepsilon}Mn_{1-\varepsilon}O_3$, [13]

$$\varepsilon = \frac{\delta}{3+\delta} \qquad (2.4)$$

A rhombohedral phase was also observed in some of these samples, shown to be stable in the composition range $0.10 \leq \delta \leq 0.18$. [14] [13] [15] One source found a decrease in the ferromagnetic coupling with the formation of this rhombohedral phase. [15]

$LaMnO_3$ Thin Films

While bulk lanthanum manganite shows only isolated ferromagnetic phases, lanthanum manganite thin films regularly show robust, consistent ferromagnetism. [10] [16] Multiple explanations have been proposed for this behavior, including interfacial polarization [5] [16], concentration of oxygen vacancies [10] [17] [18] [19]– frequently correlated to lattice strain [10] [20] - and cation deficiency [21], where the last is typically explained by invoking the canonical double exchange model, based on the presence of both Mn^{3+} and Mn^{4+} ions. Alternatively, one study explained the ferromagnetic properties of lanthanum-deficient $LaMnO_3$ by stating that some Mn^{2+} replaced the missing La^{3+}. Under

this model, ferromagnetic superexchange occurs between the A and B-site cations in addition to reducing the strain induced by the substrate. [21]

As lanthanum manganite can accommodate a wide variety of vacancies, with vacancies on the A, B or O site being stable, growth of a fully stoichiometric film is unlikely. Growing in an environment with too high a partial pressure of oxygen tends to result in cation vacancies, while too low results in oxygen vacancies. It is likely that none of these films show purely one type of vacancy, with either cation or oxygen deficiency simply being dominant. In either case, these vacancies act to reduce lattice strain.

One of the major ways thin films differ from bulk systems is the presence of significant lattice strain due to the mismatch in lattice parameter between the substrate and the film. This mismatch can be accommodated in $LaMnO_3$ through octahedral distortions or rotations or through the formation of oxygen or cation vacancies. [10] Previous studies have investigated the role of octahedral orientation on magnetic behavior in these films and showed only a slight effect, with the role of oxygen and cation vacancies playing a more substantial role. [10]

In the case of either cation or oxygen vacancies being present, the system must charge-balance to account for the missing ions. Oxygen takes only the oxidation state -2, giving oxygen vacancies an equivalent oxidation state of +2 (V_O^{+2}). This means that in a stoichiometric unit cell, $LaMnO_3$, lanthanum and manganese both take an oxidation state of +3. In this system, lanthanum is able to take an oxidation state of +2 or +3, while manganese is able to take an oxidation state of +3 or +4. For simplicity, cation vacancies

may be considered to have an oxidation state of -3 (V_{La}^{-3} or V_{Mn}^{-3}). To maintain charge neutrality, cation vacancies may be balanced through oxygen vacancies,

$$2V_c^{-3} = 3V_O^{+2} \quad (2.5)$$

conversion of manganese to a higher oxidation state,

$$V_C^{-3} = 3Mn^{+4} \quad (2.6)$$

or some combination therein. Since the presence of Mn^{+4} is what allows for ferromagnetic behavior, cationic vacancies should therefore be correlated with increasing magnetic moments. Additionally, driving oxygen into or out of the film should increase or decrease the magnetic moment respectively. Since oxygen vacancies are mobile in perovskites, this acts as a post-growth tuning parameter. This increase or decrease in magnetic moment through tuning film oxygen content has been demonstrated by several groups. [10] [17] [18] [19] [22]

3. Experimental

This section describes the samples synthesized and characterized throughout this document as well as the techniques involved in their synthesis and characterization. All films were synthesized by Mark Scaffeta.

Samples

The samples listed in table 3.1 were synthesized via molecular beam epitaxy and characterized using Rutherford backscattering spectrometry by a previous researcher. Their further characterization represents the bulk of the work presented in this document. Here forth they will be largely referred to by the sample names given here. The numbers given under "La" and "Mn" represent each element's relative abundance per formula unit; for example, a ratio of 0.8 La : 1 Mn corresponds to a film composition of $La_{0.8}MnO_3$. All samples are in the form of thin films deposited on (001) crystallized $SrTiO_3$ from MTI Corporation.

Table 3.1: List of samples by $LaMnO_3$ film cation ratios. δ represents distance from 1:1 cation stoichiometry with negative values representing manganese deficiency and positive representing lanthanum.

Sample	**La**	**Mn**	**δ**		**Sample**	**La**	**Mn**	**δ**
MS128	0.66	1	0.34		MS142	1	0.947	-0.053
MS140	0.705	1	0.295		MS138	1	0.94	-0.06
MS168	0.88	1	0.12		MS121	1	0.93	-0.07
MS170	0.9	1	0.10		MS123	1	0.89	-0.11
MS154	0.93	1	0.07		MS152	1	0.73	-0.27
MS192	1	1	0					

Synthesis and Processing

All thin films mentioned in this work were synthesized via molecular beam epitaxy. Unless otherwise mentioned, the films were annealed under vacuum immediately following deposition, as the samples cooled.

Thin Film Deposition via Molecular Beam Epitaxy (MBE)

Molecular beam epitaxy is a form of physical deposition for the epitaxial growth of thin films similar to sputtering and pulsed laser deposition. In contrast to other techniques, growth using this technique is performed under high vacuum with elemental sources and no carrier gas. As a result, growth is relatively slow and the resulting films are relatively pristine, having better purities and fewer defects than those grown by similar techniques.

Principle

All solids have some theoretical concentration of gas matching their chemical composition at their surface due to the theory of phase equilibrium:

$$M(s) \rightleftharpoons M(g) \qquad (3.1)$$

This is a negligible concentration under atmospheric pressure, being overwhelmed by the quantity of atmospheric gasses. However, on raising the temperature to increase the equilibrium partial pressure of gasceous metal and removal of atmospheric gasses through application of a vacuum this gas becomes significant, and can be used to direct, transport and re-deposit that metal atom by atom. As the gas concentration is heavily dependent on temperature, metal will be preferentially transferred from a surface at high temperature to a surface at lower temperature, with the rate being dependent on the temperature of the

hotter, source material and the difference in temperature between the source and the substrate, which the metal will be deposited on. By controlling this rate to be relatively slow, metastable phases and most other defects will have time to sublimate off, leaving only the most stable phase as a single crystal on the substrate. Using these same principles, multiple metals and oxidant gasses may be similarly introduced in fixed ratios to produce the most stable multicomponent phase.

Experimental Setup

Major components to an MBE setup include: the sources, shutters, sample and some means of determining the rate of molecular deposition, typically a quartz crystal microbalance (QCM). Various other attachments may be added, such as a small mass spectrometer for analyzing the gasses in the chamber or an electron gun for observation of the change in structure at the surface of the substrate as material is deposited.

The sources for MBE deposition were elemental metals. They were located in effusion cells at the bottom of the chamber. Each source has an individual heater capable of raising the temperature to over 1000 ^{0}C. The ports were precisely positioned and angled such that a particle travelling along their axes would strike the substrate. Additionally, various oxidant gasses could be introduced through similarly positioned tubing; a plasma source was placed at the opening of the gas delivery tube into the chamber to split the bimolecular oxidant, ex. O_2, into its molecular form, ex. O*. No shutter was available for the gas delivery tube; instead flow rate was controlled through a controller earlier along the line.

The sample holder was designed to hold a sample plate in close proximity to a tungsten filament in order to control its temperature. A thermocouple was used to track the temperature of the substrate holder. Square substrates measuring between 4 and 10 mm per side were adhered to the sample plate using a colloidal silver paint. Substrates were cleaned ultrasonically in acetone and rinsed in isopropyl alcohol. Once the substrates were adhered to the sample plate the assembly was heated on a hot plate in order to cook off any liquid in the colloidal silver.

One shutter each was located in line with the elemental metal sources, as well as one shutter in front of the substrate. The shutters could be actuated at high speed with individual motors.

The QCM was located between the source shutters and main shutter and could be wheeled into and out of position. Prior to deposition the QCM was used to determine individual deposition rates for each of the metals being used. This information was used to determine the rate of shutter actuation.

Annealing

After deposition, removal of the samples from the MBE chamber and initial characterization, the samples were annealed at 200 ^{0}C under ozone for one hour to oxidize the sample.

Characterization

Samples were characterized using various techniques to obtain information about their composition, structure and magnetic behavior.

Rutherford Backscattering Spectroscopy (RBS)

Rutherford backscattering spectroscopy is a technique for the determination of a material's composition. In this case it was used to determine the ratio of La:Mn cations present in the LMO thin films. In this technique, a beam of ions impinges on a sample, scattering elastically off the film nuclei. Because the probability of an ion scattering in this manner is proportional to the atomic weight of the atoms in the sample, composition may be determined. RBS measurements were carried out at Rutgers University.

X-ray Diffraction (XRD)

The films discussed were characterized via 1D wide angle x-ray diffraction using a Rigaku SmartLab X-Ray Diffractometer. The instrument was set up in parallel beam mode using a two-bounce Ge(220) monochromator.

Basic Principle

X-ray diffraction is a widely used technique to determine the crystal structure of a crystalline material. The basis of the technique is the concept of wave interference, or the ability of two waves to superimpose, resulting in a new amplitude. When two waves are completely in-phase this is called positive interference, and results in a signal with double the intensity of a single wave. When the two waves are exactly 90^0 out of phase they cancel eachother out entirely, resulting in zero signal. While the effects of this are negligible when considering incoherent light, when considering coherent, monochromatic light such as is

used in an X-ray diffractometer this effect can be used to resolve angstrom-level distances between periodic planes of atoms.

A crystal can be modelled as a semi-infinite series of repeating planes of atoms with interplanar spacing d. When considering an incident, monochromatic, in-phase wave striking two adjacent planes of atoms at an angle θ, it can be derived that the difference in path-length for the waves is $2d \sin(\theta)$. Given our criteria for positive interference described above, the maximum signal will be received when this quantity is equal to some multiple of the incident wave's wavelength, $n\lambda$. This leads to the first critera for a peak to be observed, Bragg's Law:

$$2d\,sin(\theta) = n\lambda \qquad (3.2)$$

In a real crystal the incident wave reflects off of all available planes, rather than just the top two. As such, Bragg's Law is insufficient to determine whether or not a peak will actually appear; two planes picked at random may give positive interference, but adding a third to the system may result in negative interference, nullifying the signal. This observation led to the formulation of the structure factor, F:

$$F_{hkl} = \sum_{j=1}^{N} f_j e^{[-2\pi i(hx_j + ky_j + lz_j)]} \qquad (3.3)$$

Where f is a scattering factor characteristic to the atom being considered, (*hkl*) are the Miller indices for the plane being considered, and (*xyz*) correspond to the coordinates of the j^{th} atom as related to its position within the unit cell of the crystal being considered. The sum is across all atoms in one unit cell. If the result of this sum is a nonzero value a peak will theoretically be present.

Experimental Setup

An x-ray diffractometer includes three major components: an x-ray source, the sample holder and a photodetector. The source must be capable of producing a high flux of in-phase, monochromatic x-rays. In this case the x-ray source was copper, which when struck by a beam of electrons produces x-rays of the characteristic wavelength 1.54 Å. As previously mentioned, the source was placed in-line with a monochromator in order to filter out any other wavelengths. In the instrument used both the source and detector could be repositioned in order to scan across a wide range of angles.

Data Analysis

As the samples were single crystals aligned at a fixed angle, parallel to the beam at 0^0, the only planes sampled were those parallel to the substrate's {001} plane. As intensity is related to the number of repeated planes and the films were much thinner than the substrate, the intensity of the film peaks were several orders of magnitude lower than those of the substrate, frequently disappearing into the background. Peak location was determined by identifying the center point between the borders at full width-half maximum.

X-ray Reflectivity (XRR)

X-ray reflectivity analysis was performed on the same instrument as discussed in the previous section. All fitting was done using GenX, a software package used for fitting x-ray diffraction data, particularly for thin films. [23]

Basic Principle

X-ray reflectivity is based on the same principle of wave interference as described in the previous section. However, in this case the waves being measured are not bouncing off adjacent planes of atoms but are instead being reflected off the interfaces between the film and the air and the substrate and film. The location of intensity maxima may still be determined using Bragg's Law, substituting the interplanar distance for the film thickness.

Experimental Setup

This technique is used on the same instrument as described in the previous section. The x-ray source and detector are panned through $2\theta = \sim 0\text{-}5^0$, obtaining an intensity profile similar to that shown in Figure 3.1. At 0^0 the source points directly into the detector, returning half the straight-through beam intensity. At $\sim 0.4^0$ the intensity rises up to the leading edge then begins falling with periodic fringes, called Keissig fringes. By around 5^0, depending on the sample, intensity has returned to zero with some background noise.

Data Analysis

The location of the leading edge, the background intensity and the position and spacing between Keissig fringes can be accurately determined through various models using input parameters of the density of your materials, the volume of a unit cell, the thickness and roughness of each layer, in this case the thin film and the substrate, and some properties of the instrument used such as beam intensity

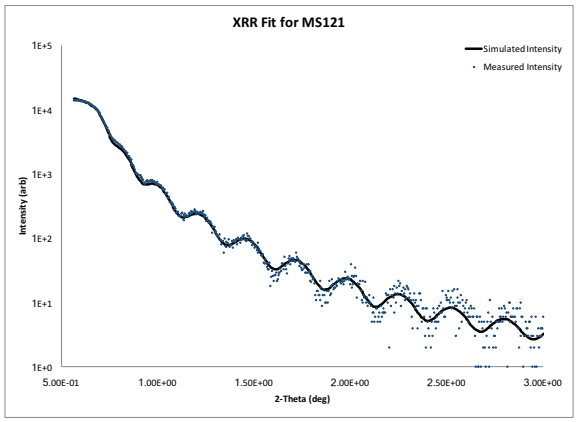

Figure 3.1 Sample XRR data with simulated fit. Data is shown as points, fit is shown as line.

and background noise. The software package GenX incorporates these models to generate an XRR profile which can then be fitted to real data to determine film thickness and roughness.

Vibrating Sample Magnetometry

The films were characterized using a Quantum Design Physical Property Measurement System (PPMS) with added Vibrating Sample Magnetometer (VSM). Measurements were taken using the onboard software and analyzed in Microsoft Excel.

Basic Principle

The principle underlying VSM is that of electromagnetic induction: the ability for an electric potential to be produced in a material due to its interaction with a changing magnetic field. The magnitude of the field produced is a direct function of the rate of change of the magnetic flux. By rapidly moving a magnetized sample past a coil of wire a potential may be induced in direct proportion to the magnetization of the sample, for some constant sample velocity. This potential may then be measured and the sample magnetization obtained.

Experimental Setup

The sample chamber is a sealed volume purged with helium and held under vacuum to prevent background magnetization from impurity gasses. The samples were affixed to a quartz rod using conductive carbon tape, which was in turn affixed to a stiff rod which was

mounted to the motor used to vibrate the sample. This quartz rod hung suspended within two coils of copper wire.

In order to obtain field (M) vs moment (H) loops, the chamber was cooled to 10 K under an applied field of 0.05 T. The sample was then vibrated at 40 Hz past the pickup coil as the applied field was varied from 0 T -> +1 T -> -1 T -> +1 T. The field was then reduced to 0.1 T and measurements were obtained at constant time intervals as the chamber was warmed to 300 K in order to obtain a plot of moment vs temperature.

Data Analysis

The magnetic moment data obtained from this test is in units of emu, or erg per gauss, and is the net magnetic moment for the entire sample, not just the film. The quartz rod and carbon tape used have no net magnetic moment, but strontium titanate (STO) is diamagnetic under all temperatures sampled. Additionally, it is more useful to have magnetic moment in a physically meaningful unit. Therefore, the substrate moment is removed from the net moment and the moment is converted to Bohr magnetons per manganese atom, a value corresponding to the average number of unpaired electrons per manganese atom aligned in the direction of the applied field.

The method of determining the substrate moment from the net moment varies depending on the measurement being taken. In the case of measuring moment as a function of temperature under a constant field the magnetization of the substrate can be taken as a constant equal to the average magnetization near room temperature – or, above the transition temperature for LMO, T_C, and subtracted from the net moment,

(3.4)

$$\mu_{STO} = \frac{1}{n} \sum_{T_i = T_C + c}^{n} \mu_i$$

for T_n = 300 K and c some constant > 20. In the case of taking moment measurements as a function of the applied field, LMO eventually reaches some saturation moment while the moment of STO continues to decrease. Therefore, the magnetic moment of STO can be assumed to have a linear relationship to the applied field, M, with a slope, a, equal to the slope obtained at applied fields above the field required to saturate LMO and an intercept of zero.

$$\mu_{STO} = a * M \quad (3.5)$$

Once obtained, these values may be subtracted from the net magnetic moment to obtain the film moment through the simple relationship:

$$\mu_{film} = \mu_{net} - \mu_{STO} \quad (3.6)$$

This moment may then be normalized by the volume of the film, x and y dimensions determined through caliper measurements, thickness determined through XRR, multiplied by the volume per manganese atom, determined by the volume of a unit cell, and converted to Bohr magnetons using the relationship 1 $\mu_B = 9.274 \times 10^{-21}$ erg/G.

4. Results and Discussion

Structural Analysis

The samples were analyzed using X-ray diffraction to draw conclusions about the crystal structure of the films. Additionally, X-ray reflectivity measurements were performed to determine their thickness. The intensities for each film were normalized by the maximum obtained intensity for that sample, obtained from the substrate, so they could be easily compared. For details and film compositions refer to the Experimental section.

X-Ray Diffraction

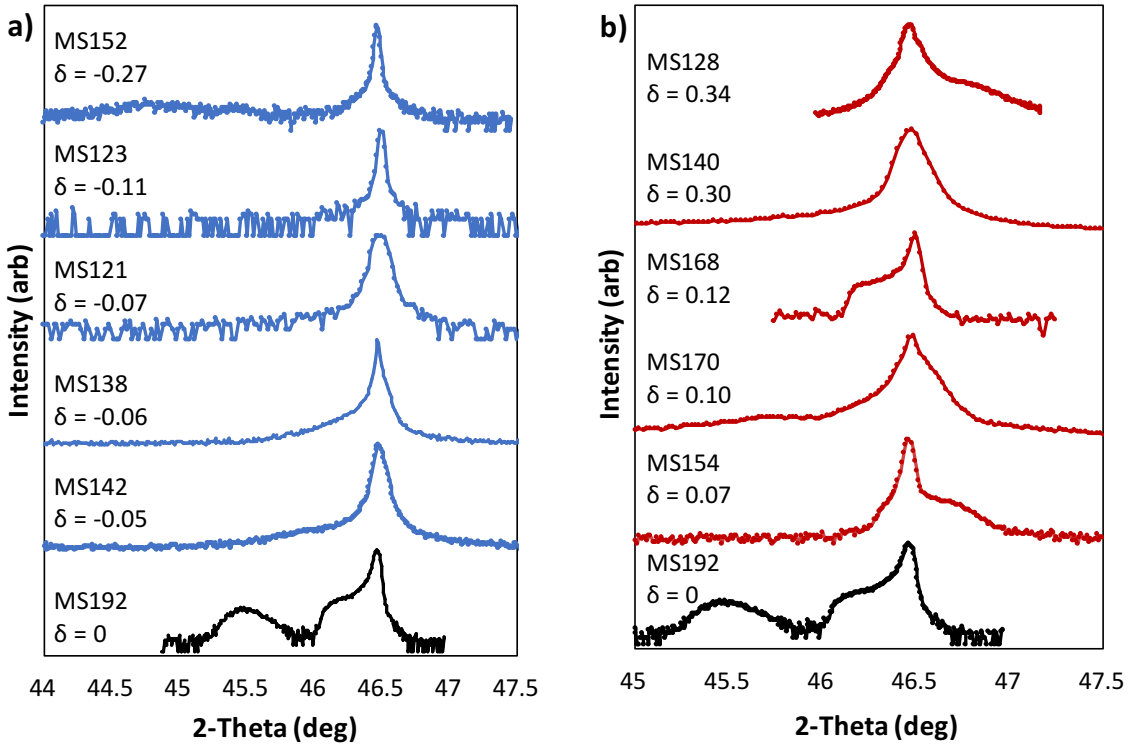

Figure 4.1: X-ray diffraction data for $LaMnO_3$ films on $SrTiO_3$, at angles near the (002) peak for the $SrTiO_3$ substrate. This $SrTiO_3$ peak occurs at much higher intensity than the film peaks (10^3-10^6), at approximately 46.47^0.

The substrate, $SrTiO_3$, shows a peak at 46.46^0, corresponding to the (002) peak, assuming the equilibrium cubic structure with a lattice parameter of 3.905 Å. The films analyzed showed similar lattice parameters if they showed a peak at all.

Only a handful of samples showed distinct film peaks when analyzed via x-ray diffraction. This could be the result of various factors including film quality or having a lattice parameter which closely matches the substrate. A literature survey also reveals that obtaining a high intensity, resolved peak for this film/substrate combination is unlikely, owing largely to the close match between the lattice parameters of the film and substrate. [17] [18] [19]

From these graphs, some initial conclusions can be made. For one, the stoichiometric film, MS192, produced a much narrower, higher intensity, resolved peak than any other film, with a maximum intensity of 0.18% of the intensity of the substrate peak. This is compared to the next highest intensity resolved peak, that obtained from MS152, with a maximum intensity of 0.026% of the intensity of the substrate peak. This may be coincidental, further study may or may not verify this result. Additionally, manganese-deficient films typically displayed peaks at lower angles than their lanthanum-deficient counterparts, suggesting these films exhibit larger c-axis parameters. Similarly, the location of lanthanum-deficient film peaks which overlap the substrate peak suggests these films were more easily able to accommodate the induced strain through structural changes. It should be noted that film MS170, unlike the rest of the lanthanum-deficient films, showed a peak near 45.75^0, corresponding to a lattice parameter of 3.966 Å, which may explain its anomalous magnetic behavior discussed later.

While many of the film peaks overlapped the substrate peak, it was possible to make an estimate of their position. Where the peak was resolved, the peak location and width was evaluated at full width-half maximum: the difference between the angles at which the peak reached half its maximum intensity was taken as the width, and the peak was considered to be at exactly the center of this range. Where the film peak overlapped the substrate peak, the peak location was considered to be where the intensity showed the smallest change with regards to theta ($\frac{dI}{d\theta}$ was at a minimum). Width was then calculated by doubling the distance to the point at which intensity had decreased by half. Lattice parameter was calculated using Bragg's law. Strain was calculated as the fractional difference in bond length between substrate and film lattice parameters, using the substrate lattice parameter as a baseline.

Table 4.1 Summary of x-ray diffraction results. Peak width is calculated at half maximum. Film peak intensity is calculated as a percentage of substrate peak intensity. Positive strain corresponds to compression, while negative corresponds to tension.

		Substrate		Film				
Sample	δ	Peak Location	c-lattice parameter (Å)	Peak Location	c-lattice parameter (Å)	Peak Intensity	Peak Width	Strain
MS152	-0.27	46.469^0	3.908	44.825^0	4.044	0.026%	0.385^0	0.035
MS123	-0.11	46.495^0	3.906					
MS121	-0.07	46.500^0	3.906					
MS138	-0.06	46.469^0	3.908					
MS142	-0.053	46.479^0	3.907	45.959^0	3.949	0.0085%	0.320^0	0.011
MS192	0.00	46.463^0	3.909	45.492^0	3.988	0.18%	0.205^0	0.020
MS154	0.07	46.469^0	3.908	46.809^0	3.881	0.028%	0.180^0	-0.0069
MS170	0.10	46.489^0	3.907	45.749^0	3.966	0.012%	0.560^0	0.015
MS168	0.12	46.497^0	3.906	46.242^0	3.926	0.32%	0.150^0	0.0051
MS140	0.295	46.480^0	3.907					
MS128	0.34	46.478^0	3.908	46.754^0	3.886	0.16%	0.239^0	-0.0056

Effect of Annealing

Ozone Anneal

Several samples were annealed in ozone to maximize their oxygen content. For details refer to the Annealing subsection of the Experimental section. The effect of this anneal on their structure was minimal, causing only slight changes to the position and intensity of observed film peaks, shown in the figure below.

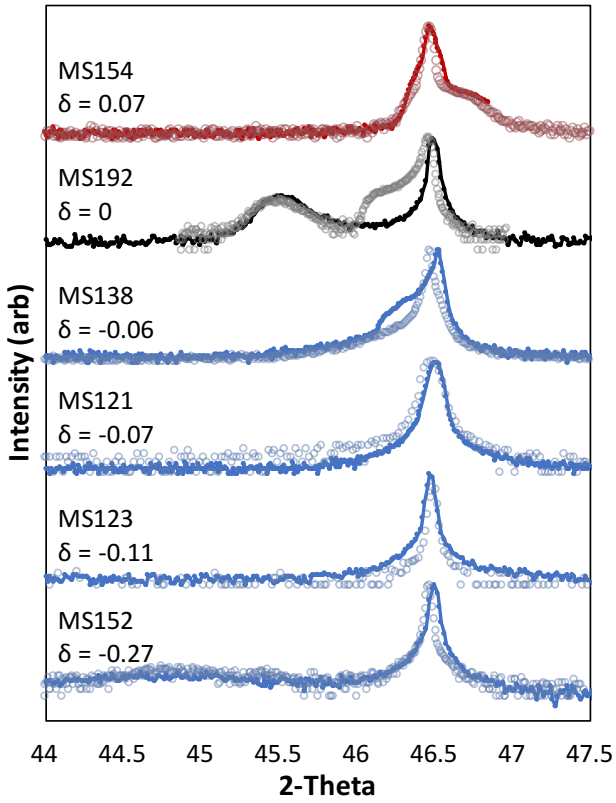

Figure 4.2 X-ray diffraction peaks following ozone annealing. Pre-anneal spectra are shown with open circles.

Of interest are samples MS192 and MS138, which showed sizeable low-angle shoulders adjacent to the film peak prior to annealing which largely disappeared. This

behavior is consistent with W. S. Choi's work on annealing LaMnO3 thin films in an oxygen-reducing environment, in which the shoulder shifted to lower angles following an anneal to reduce the oxidation state of the films. [17] [18] A representative result is shown to the right, repurposed from [18]. Sample A is the film in the as-grown condition, sample B is following an anneal under 96% argon and 4% hydrogen at 500 ^{0}C. Samples C, D and E were annealed at 700 ^{0}C for 1h, 900 ^{0}C for 1h and 900 ^{0}C for 3h, respectively.

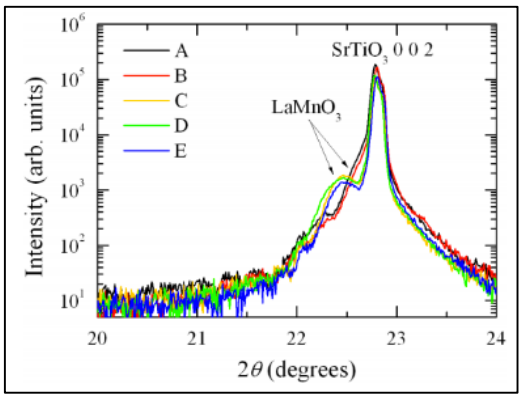

Figure 4.3 XRD spectra for LaMnO3 near the (001) substrate peak, repurposed from [18].

X-Ray Reflectivity

The samples were analyzed using x-ray reflectivity to determine their thickness, which was used in the determination of volume; results are compiled in the table below. Number of unit cells was calculated with an assumed c-lattice parameter of 3.905 Å. Volume was calculated by multiplying thickness by film area, dimensions determined through caliper measurement. For further details refer to the experimental section.

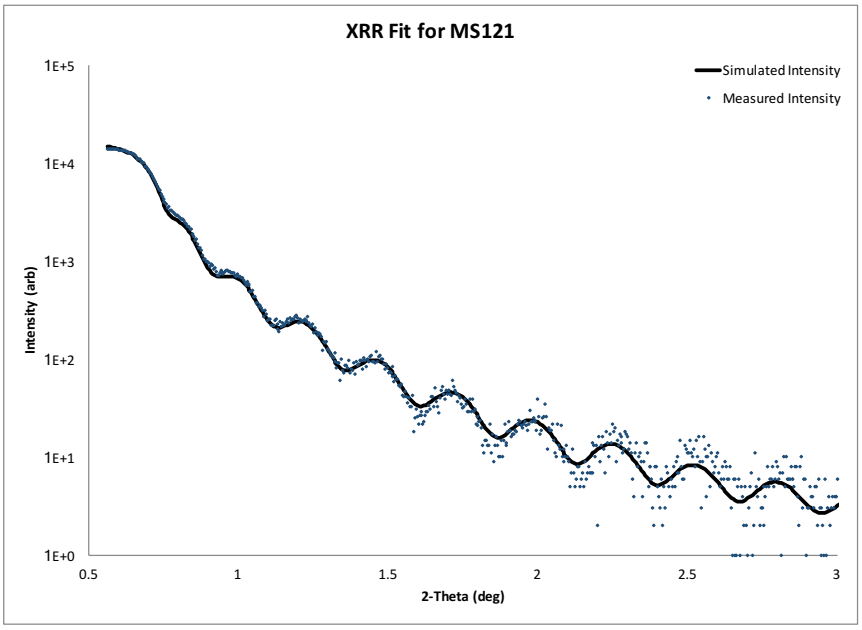

Figure 4.4 Sample fit of x-ray reflectivity data. Intensity is on the Y axis, 2θ is on the X. Blue points represent the raw data, red line represents the simulated intensity. The difference between the actual and simulated data is shown in the sub-graph (bottom).

Table 4.2 Film thickness as obtained through x-ray reflectivity analysis

Film	Thickness (Å)	Thickness (UC)	Volume (mm^3)
MS121	311	79.6	0.000544
MS123	327	83.7	0.000706
MS128	405	103.7	0.00133
MS138	204	53.3	0.00133
MS140	186	47.6	0.000610
MS142	230	58.9	0.000652
MS152	374	95.8	0.000895
MS154	398	101.9	0.000773
MS168	429	109.9	0.00124
MS170	450	115.2	0.00110
MS192	472	120.9	0.00116

Magnetic Behavior

The films were characterized using vibrating sample magnetometry to observe their magnetic behavior in response to changes in both field strength and temperature. For details see the experimental section.

Moment vs Applied Field (MvH)

As-Grown Results

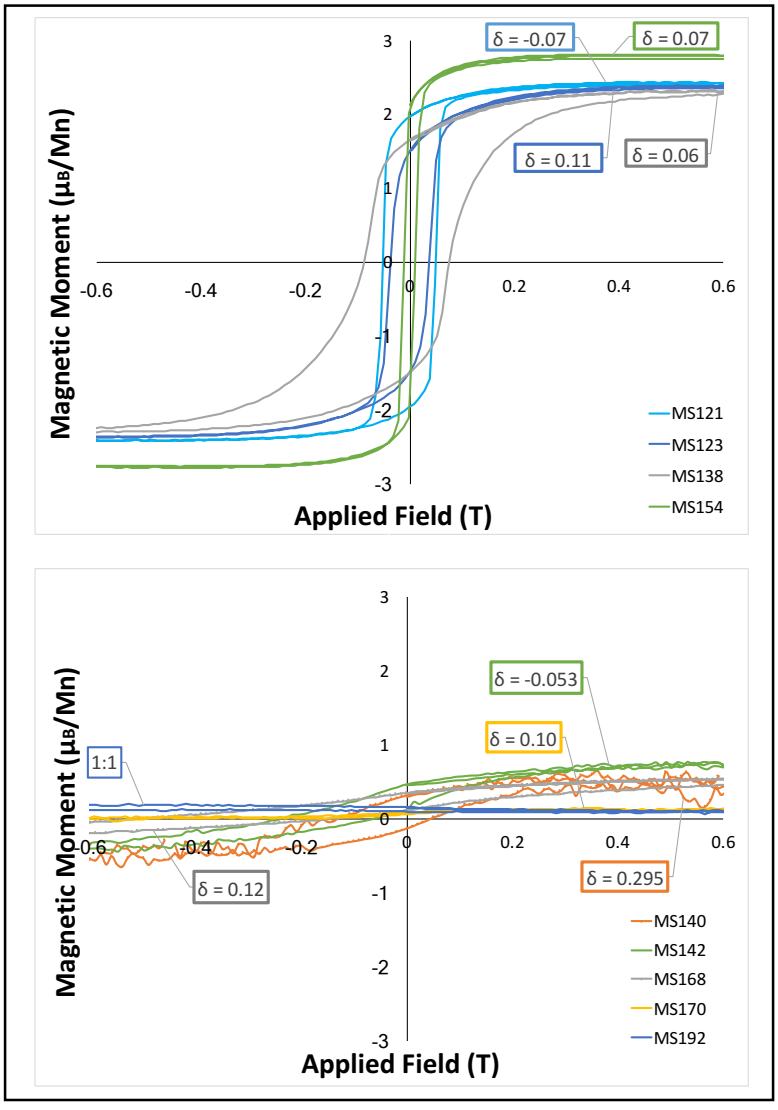

Figure 4.5 Magnetization vs applied field at 10K for $LaMnO_3$ films, divided by magnitude of film moment.

Two distinct types of behavior are observed, hereafter referred to as ferromagnetic and antiferromagnetic, where ferromagnetic refers to a saturation magnetic moment of >1 μ_B/Mn and antiferromagnetic refers to a saturation magnetic moment of <1 μ_B/Mn. The films displaying ferromagnetic behavior show typical hysteresis loops with well-defined coercivity and saturation moments; conversely, the antiferromagnetic films show extremely distorted hysteresis loops sometimes responding opposite to the applied field, and all shifted toward positive magnetization. The magnitude of the saturation moments of MS170 and MS192 are consistent with spin canting in the antiferromagnetic phase, typically assigned a value of 0.18 μ_B/Mn. [24] [25] The positive shift is consistent with the findings of Matsumoto [11], that a residual moment exists in the direction of field cooling.

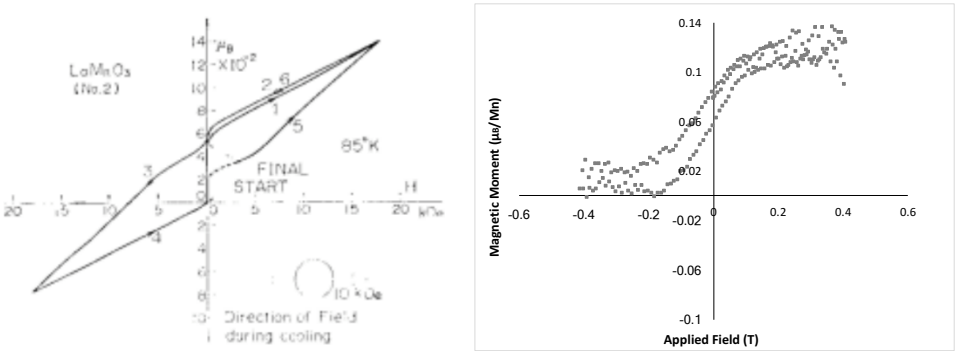

Figure 4.6 Comparison of AF sample to AF behavior reported in [11]. Both samples show a small, residual magnetic moment in the direction of field cooling.

A cursory evaluation shows no relationship between saturation magnetic moment and thickness, shown in Figure 4.7. An argument could be made that ferromagnetism is more likely for film thicknesses between 60 and 100 unit cells, however there is no physical basis for this claim. This does not rule out the possibility of a ferromagnetic transition occurring at low thickness as all films measured were substantially thicker than those

analyzed in Wang et. al., those films being between 2 and 24 unit cells in thickness. [24] The compositional relationship to applied field is unclear in these graphs and explored further in Figures 4.8-4.9.

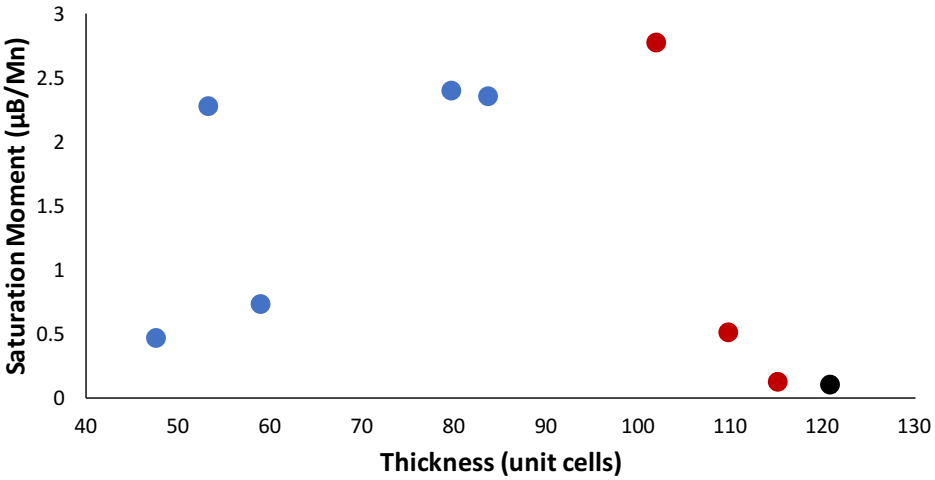

Figure 4.7 Saturation magnetic moment vs thickness for $LaMnO_3$ films on $SrTiO_3$

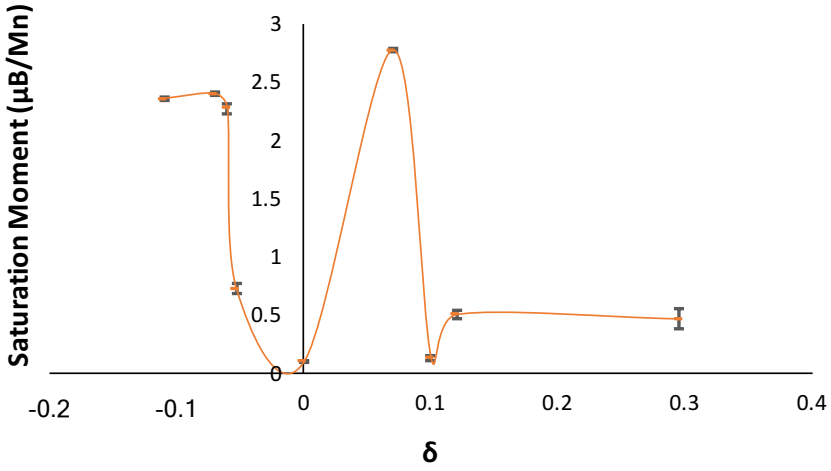

Figure 4.8 Saturation magnetic moment as a function of composition. Error calculated by summing per-measurement error and error between measurements within the saturation region of the moment vs field measurements.

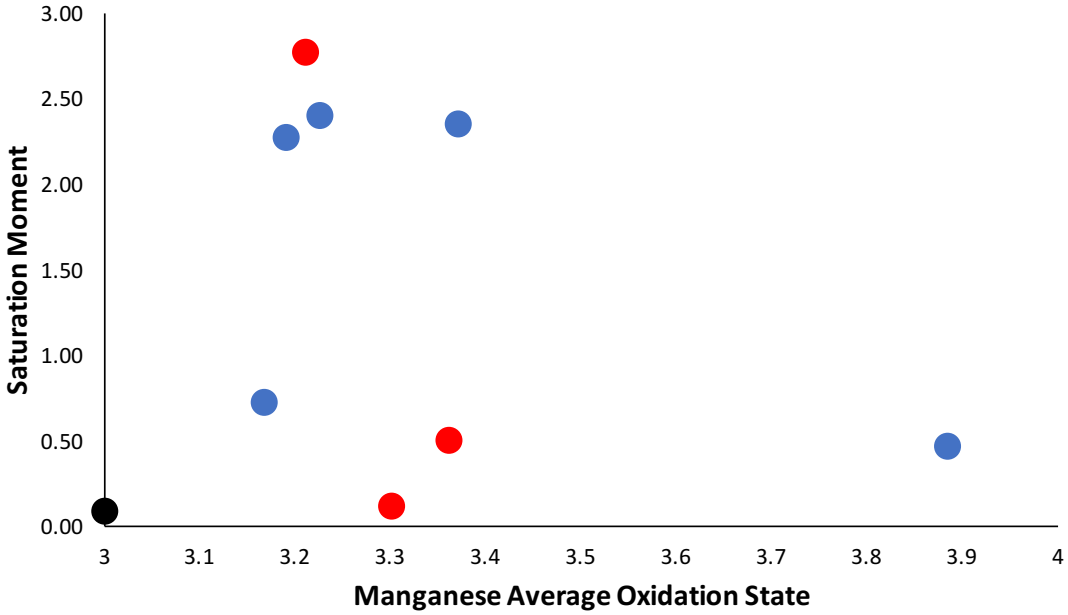

Figure 4.9 Saturation moment as a function of manganese valence state, assuming no oxygen vacancies are present. Red points indicate lanthanum deficiency while blue points indicate manganese deficiency. The black point corresponds to the stoichiometric film measured. In non-stoichiometric $LaMnO_3$, manganese can have an oxidation state of +3 or +4.

Analysis of saturation moment as a function of composition shows a striking composition dependence, with the film exhibiting antiferromagnetic behavior at near stoichiometric conditions ($\delta \approx \pm 0.05$) and ferromagnetic in the range slightly beyond that ($0.05 \leq \delta \leq 0.15$), returning to antiferromagnetic for larger values of δ. Converting stoichiometric imbalance to manganese oxidation state, assuming all charge imbalance is accommodated through oxidation of manganese and that the films are fully oxidized (three oxygen atoms per formula unit), this pattern becomes even more clear, as seen in Figure 4.9.

This trend mirrors what is seen in the $LaMnO_3$-$SrMnO_3$ phase diagram of magnetic properties [26], which shows antiferromagnetic behavior at compositions for which the oxidation state of manganese is close to 3 or 4 and ferromagnetic behavior for oxidation states in the range of 3.2 to 3.6. This suggests cation deficiency as an alternative tuning parameter to strontium substitution when tuning lanthanum manganite from antiferromagnetic to ferromagnetic.

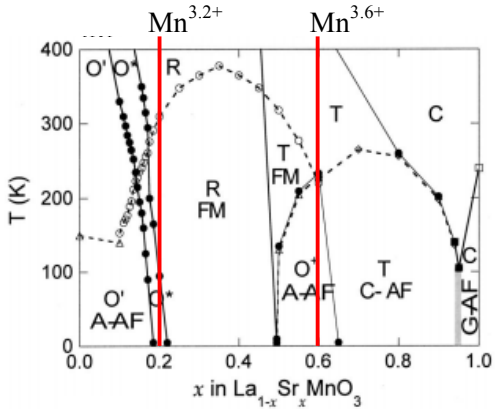

Figure 4.10 Phase diagram for strontium-doped $LaMnO_3$. A-AF, C-AF and G-AF represent different types of antiferromagnetic ordering, while FM represents ferromagnetic ordering. C, T, R and O refer to cubic, tetragonal, rhombohedral and orthorhombic symmetries, respectively. Repurposed from [28]

The lanthanum-deficient samples measured do not appear to follow the valence vs magnetic behavior trend seen in Figure 4.10, showing an early transition to the antiferromagnetic phase. Additionally, the ferromagnetic lanthanum-deficient sample, MS154 ($\delta = 0.10$), shows a much higher transition temperature than the others, discussed in the next section. These two behaviors suggest much higher oxidation states than would be explained by examining their cation-deficiency alone, which cannot be explained through oxygen nonstoichiometry. It is possible these films show phase separation and/or substitutional manganese on the A-site. Further work should be done to determine the actual oxidation state of the manganese in these films.

Annealing

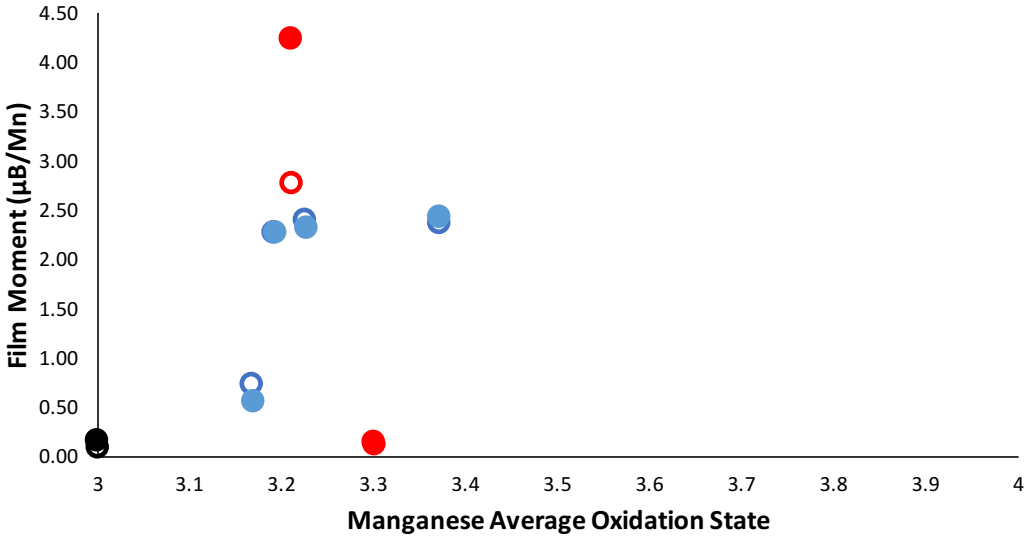

Figure 4.11 Change in saturation magnetic moment due to ozone annealing, as a function of manganese average oxidation state. Red points indicate lanthanum deficiency while blue points indicate manganese deficiency.

Annealing the films in ozone increased the films' magnetic moments in 5 of 7 cases, consistent with various findings showing ferromagnetic behavior in fully oxidized samples and antiferromagnetic behavior in fully reduced films. [10] In the films showing ferromagnetic behavior this typically accounted for an increase of <10%. The fractional change in moment for AF films was higher, but never increased a moment from below 1 μ_B to above it.

Analysis of the literature suggests much larger changes are possible, including tuning from antiferromagnetic to ferromagnetic and back. However, this effect would only be seen if the annealing process substantially affected the concentration of oxygen vacancies and therefore the oxidation state of the manganese. Further work should be done to determine the effect of annealing in a reducing environment on the magnetic behavior of the films.

Moment vs Temperature and the Paramagnetic Transition Temperature

As-Grown

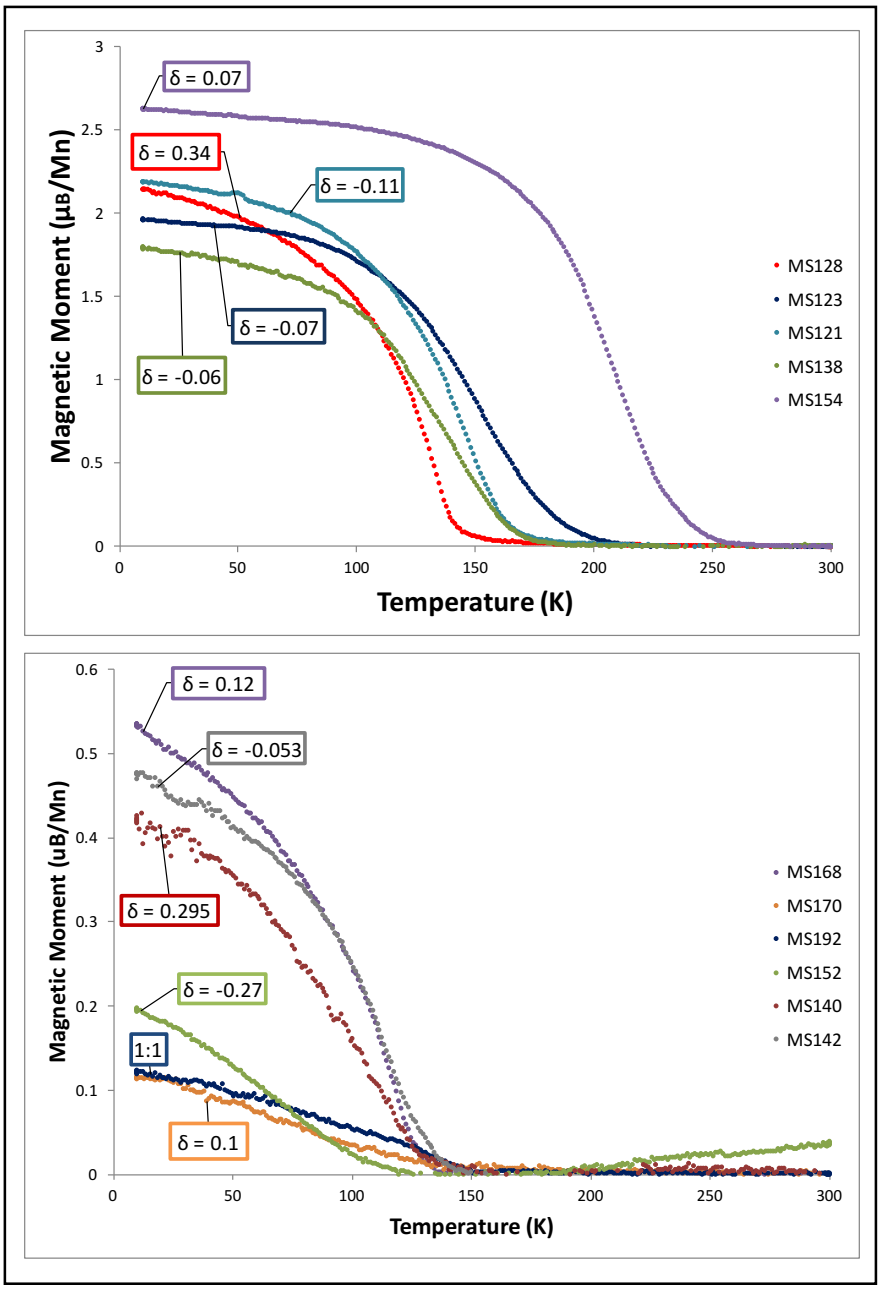

Figure 4.12 Film moment vs temperature under an applied field of 0.1 T

The films showed consistent moment vs temperature behavior, transitioning to a paramagnetic phase at temperatures between 110 K and 190 K, with one outlier showing a transition temperature at 237 K. This is consistent with the findings in [26] that lanthanum deficiency leads to a dramatically increased transition temperature. Transition temperatures were obtained via trend line, summarized in the table below.

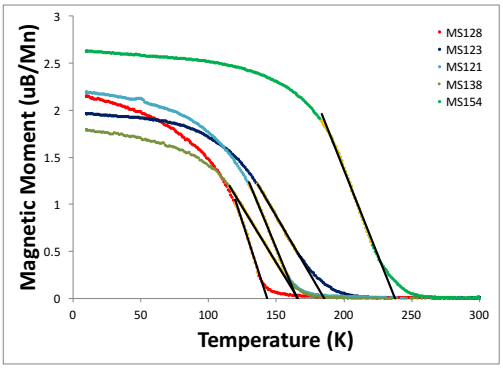

Figure 4.13 Determination of transition temperature via trend line.

Table 4.3 Transition temperatures for all films in which moment vs temperature was measured

	δ	**Mn Valence**	**Film Moment at 10K**	**Transition Temperature (K)**
MS152	-0.27	4.11	0.197	111
MS123	-0.11	3.37	1.96	185
MS121	-0.07	3.23	2.19	165
MS138	-0.06	3.19	1.85	166
MS142	-0.053	3.17	0.626	134
MS192	0	3.00	0.123	161
MS154	0.07	3.21	2.63	237
MS170	0.1	3.3	0.117	150
MS140	0.295	3.89	0.302	135
MS128	0.34	4.02	2.15	143

The average transition temperature was 159 K. Upon exclusion of the samples with nonphysical manganese valence states (oxidation state <3 or >4), the transition temperature is 167 K. Further excluding the sample with a very high transition temperature, MS154,

the average transition temperature is 157 K. While the films showing large magnetic moments at 10K exhibited a greater variation in transition temperature, no correlation was observed between film moment and transition temperature. Additionally, no clear relationship was found between manganese oxidation state and transition temperature or film thickness and transition temperature.

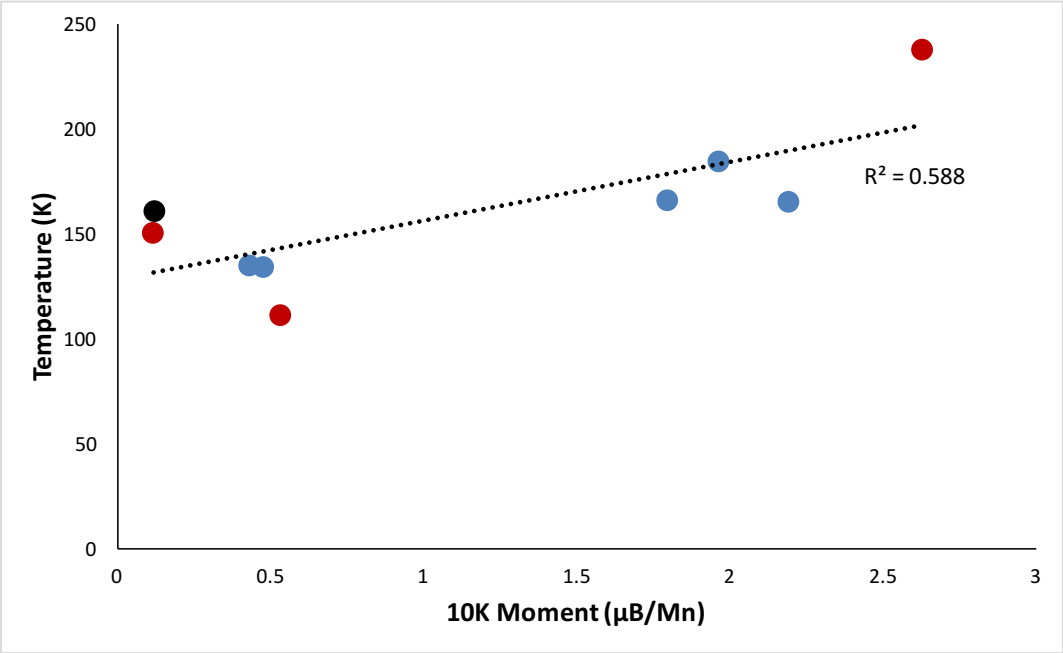

Figure 4.14 Film moment at 10K under an applied field of 0.1 T vs transition temperature, evaluated via trend line. Red points indicate lanthanum deficiency while blue points indicate manganese deficiency. No correlation was found.

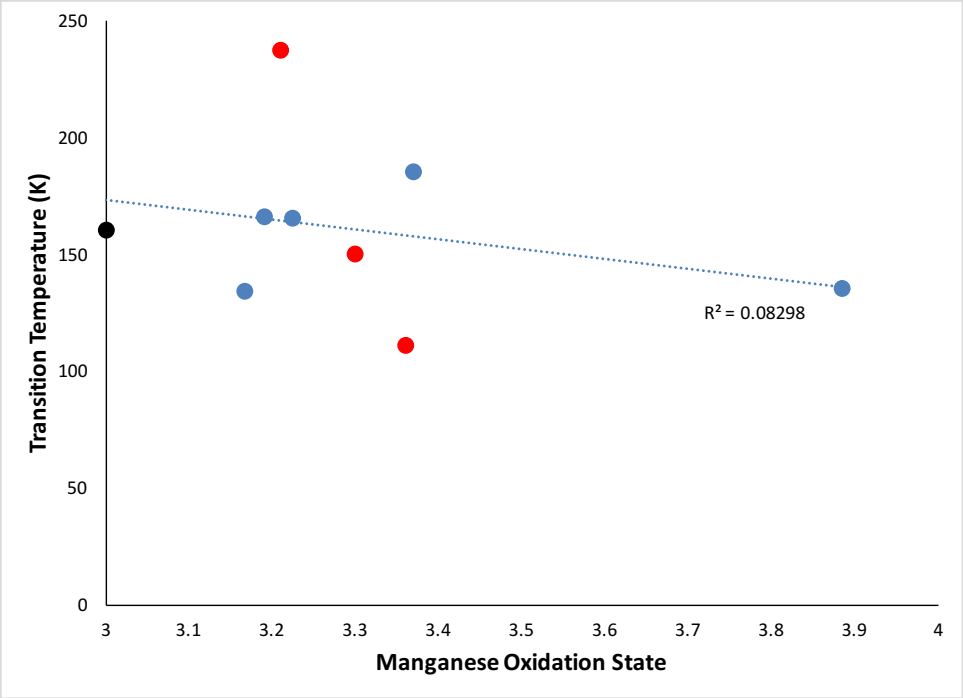

Figure 4.15 Manganese oxidation state vs transition temperature. Red points indicate lanthanum deficiency while blue points indicate manganese deficiency. Oxidation state determined assuming 3 oxygens of valence -2 and lanthanum of valence +3. No correlation was found.

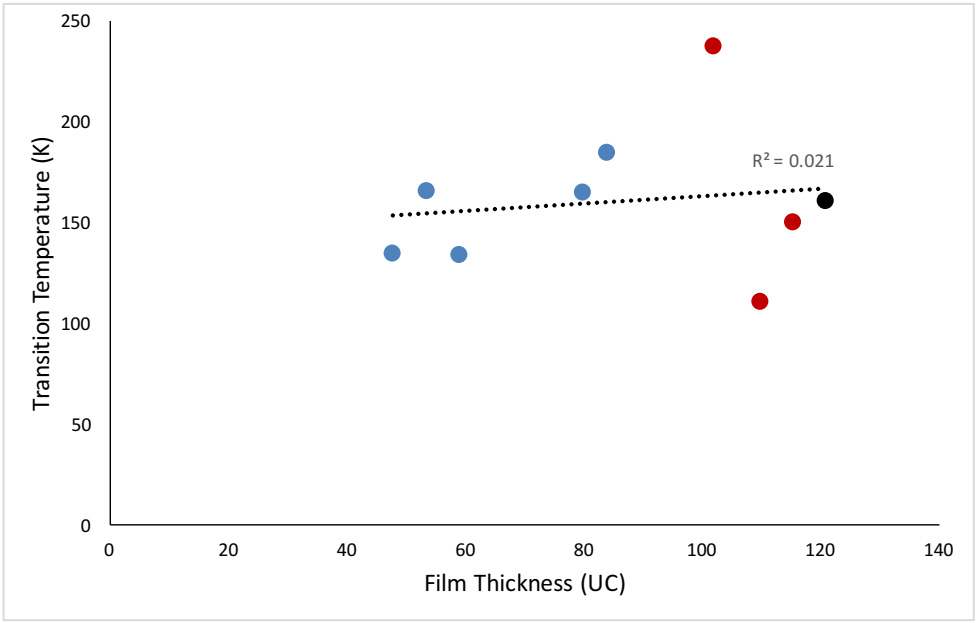

Figure 4.16 Film thickness vs transition temperature. Red points indicate lanthanum deficiency while blue points indicate manganese deficiency. Thickness determined from x-ray reflectivity; number of unit cells based on a lattice parameter of 3.905 Å. No correlation was found.

Annealing

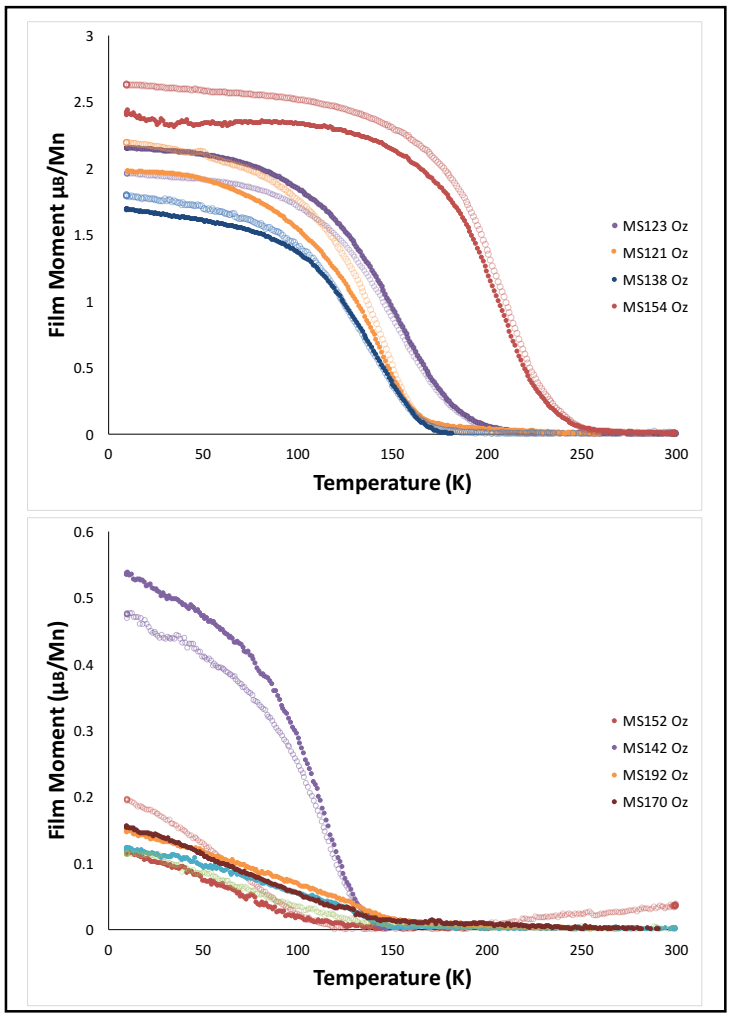

Figure 4.17 Film moment vs temperature for a constant applied field of 0.1 T, following annealing in ozone at 200 ^{0}C for 1h. Pre-anneal behavior is shown as open circles. The apparent smaller moment in several films is due to a much higher room temperature film moment, which was subtracted out as described in the experimental section.

Annealing in ozone had no appreciable effect on the moment vs. temperature behavior of the films analyzed. However, several films showed a much higher room temperature magnetic moment following this annealing step. This is inconsistent with findings that oxidizing the films causes a dramatic increase in transition temperature. One potential explanation for this is that the films were already fully oxidized, as discussed in the previous section.

5. Conclusion and Future Work

A systematic study of cation-deficient lanthanum manganite thin films deposited via molecular beam epitaxy was undertaken. The films were characterized structurally and in terms of magnetic behavior. Four films exhibited robust ferromagnetic behavior while six exhibited antiferromagnetic behavior. The range of manganese oxidation states corresponding to ferromagnetic behavior, assuming all cation deficiency was accounted for through oxidation of manganese, was consistent with the established phase diagram for $La_{1-x}Sr_xMnO_3$, assuming, again, all charge imbalance due to the substitutional strontium was accounted for through oxidation of manganese.

Some unexpected behavior was seen in the lanthanum-deficient films, including an antiferromagnetic sample which should have been within the range of ferromagnetic samples and a sample showing a magnetic moment of more than 4 μ_B/Mn, assuming all contributions to the moment were due to the manganese atoms. This could be explained through the presence of a secondary $Mn^{+2}Mn^{+3}O_3$ phase, in which manganese takes the role of an A-site substitutional group, or phase separation into two phases with radically different oxidation states of the manganese atom. Future studies should be done to determine the relative stability of lanthanum vacancies and manganese substitutions, as well as directly observe the oxidation state of the manganese in these films.

Annealing the films in an oxidizing environment showed a consistent increase in their magnetic moment, consistent with the hypothesis that oxygen vacancies are an alternative means of charge-balancing this material which suppresses the ferromagnetism present in cation-deficient films. However, the change in magnetic moment was generally

minimal, suggesting cation composition is still the most important factor at play when determining the magnetic behavior of these films, and that the as-grown films were already nearly fully oxidized.

Works Cited

[1] C. Walter, "Kryder's Law," *Scientific American,* 1 August 2005.

[2] D. Rosenthal, "DSHR's Blog," 2 4 2014. [Online]. Available: http://blog.dshr.org/2014/04/evercloud-workshop.html.

[3] P. McCray, "Leaping Robot Blog," 4 2014. [Online]. Available: http://www.patrickmccray.com/2014/04/.

[4] S. Piramanayagam, "Perpendicular Recording Media for Hard Disk Drives," *Journal of Applied Physics,* vol. 102, p. 011301, 2007.

[5] J. J. Peng et. al., "Restoring the magnetism of ultrathin $LaMnO_3$ films by surface symmetry engineering," *Physical Review B,* vol. 94, no. 214404, pp. 1-6, 2016.

[6] C. Kittel, Introduction to Solid State Physics, 8th Edition, Wiley, 2005.

[7] Y. Ren et. al., "Temperature-induced magnetization reversal in a YVO_3 single crystal," *Nature,* vol. 396, pp. 441-444, 1998.

[8] A. Bhattacharya and S. J. May, "Magnetic Oxide Heterostructures," *Annu. Rev. Mater. Res.,* vol. 44, pp. 65-90, 2014.

[9] M. A. Peña and J. L. G. Fierro, "Chemical Structures and Performance of Perovskite Oxides," *Chem. Rev.,* vol. 101, pp. 1981-2017, 2001.

[10] J. Roqueta et. al., "Strain-Engineered Ferromagnetism in $LaMnO_3$ Thin Films," *Crystal Growth & Design,* vol. 15, no. 11, pp. 5332-5337, 2015.

[11] G. Matsumoto, "Study of $(La_{1-x}Ca_x)MnO_3$. I. Magnetic Structure of $LaMnO_3$," *Journal of the Physical Society of Japan,* vol. 29, no. 3, pp. 606-614.

[12] O. H. Hansteen et. al., "Divalent manganese in reduced $LaMnO_{3-\delta}$—effect of oxygen nonstoichiometry on structural and magnetic properties," *Solid State Sciences,* vol. 6, pp. 279-285, 2004.

[13] J. Töpfer and J. B. Goodenough, "$LaMnO_{3+\delta}$ Revisited," *Journal of Solid State Chemistry,* vol. 130, pp. 117-128, 1997.

[14] F. J. Palomares et. al., "Temperature dependence of the magnetic properties in $LaMnO_{3+\delta}$," *Journal of Applied Physics,* vol. 99, p. 08A702, 2006.

[15] C. Ritter et. al., "Influence of oxygen content on the structural, magnetotransport, and magnetic properties of $LaMnO_{3+\delta}$," *Physical Review B,* vol. 56, no. 14, pp. 8902-8911, 1997.

[16] X. Renshaw Wang et. al., "Imaging and control of ferromagnetism in $LaMnO_3/SrTiO_3$ heterostructures," *Science,* vol. 349, no. 6249, pp. 716-719, 2015.

[17] W. S. Choi et. al., "Effects of oxygen-reducing atmosphere annealing on $LaMnO_3$ epitaxial thin films," *Journal of Physics D: Applied Physics,* vol. 42, p. 165401, 2009.

[18] W. S. Choi et. al., "$LaMnO_3$ Thin Films Grown by Using Pulsed Laser Deposition and Their Simple Recovery to a Stoichiometric Phase by Annealing," *Journal of the Korean Physical Society,* vol. 58, no. 3, pp. 569-574, 2011.

[19] H. S. Kim and H. M. Christen, "Controlling the magnetic properties of $LaMnO_3$ thin films on $SrTiO_3(100)$ by deposition in a O_2/Ar gas mixture," *Journal of Physics: Condensed Matter,* vol. 22, p. 146007, 2010.

[20] K. H. Ahn and A. J. Millis, "Effects of in-plane strain on orbital ordering and magnetism in $LaMnO_3$ thin film," *Physica B,* Vols. 312-313, pp. 766-768, 2002.

[21] A. Galdi et. al., "Magnetic properties and orbital anisotropy driven by Mn^{2+} in nonstoichiometric $La_xMnO_{3-\delta}$ thin films," *Physical Review B,* vol. 83, no. 064418, pp. 1-7, 2011.

[22] A. Gupta et. al., "Growth and giant magnetoresistance properties of La-deficient $La_xMnO_{3-\delta}$ ($0.67<x<1$) films," *Applied Physics Letters,* vol. 67, no. 23, pp. 3494-3496, 1995.

[23] M. Björck, "GenX," 18 10 2016. [Online]. Available: http://genx.sourceforge.net/.

[24] X. Renshaw Wang et. al., "Imaging and control of ferromagnetism in $LaMnO_3/SrTiO_3$ heterostructures," *Science,* vol. 349, no. 6249, pp. 716-719, 2015.

[25] V. Skumryev et. al., "Weak ferromagnetism in $LaMnO_3$," *The European Physical Journal B,* vol. 11, pp. 401-406, 1999.

[26] S. J. Kim et. al., "Influence of La defect on the magnetoresistance and magnetic properties of $La_{1-x}MnO_3$," *Journal of Applied Physics,* vol. 89, no. 11, pp. 7416-7418, 2001.

[27] Y. Tokura and N. Nagaosa, "Physics in Transition-Metal Oxides," *Science,* vol. 288, no. 5465, p. 462, 2000.

[28] O. Chmaissem et. al., "Structural and magnetic phase diagrams of $La_{1-x}Sr_xMnO_3$ and $Pr_{1-y}Sr_yMnO_3$," *Physical Review B,* vol. 67, p. 094431, 2003.